Planar Defects

24

CHAPTER PREVIEW

Internal interfaces (grain boundaries, phase boundaries, stacking faults) or external interfaces (i.e., surfaces) are perhaps the most important defects in crystalline engineering materials. Their common feature is that we can usually think of them as all being two-dimensional, or planar, defects. The main topics of this chapter will be:

- Characterizing which type of internal interface we have and determining its main parameters.
- Identifying lattice translations at these interfaces from the appearance of the diffraction-contrast images.

D. B. Williams et al., *Transmission Electron Microscopy*

Rotations are usually associated with line defects and they will be discussed in Chapter 25. We can't usually identify the details of the local structure of an interface unless we use HRTEM, so we will return to that topic in Chapter 28.

Planar Defects

24

24.1. TRANSLATIONS AND ROTATIONS

An interface is simply a surface which separates any two distinct regions of the microstructure. For most of our discussion, we will assume that the surface is flat and is thus a planar defect. We can sketch a general interface as shown in Figure 24.1.

> The upper crystal is held fixed while the lower one is translated by a vector **R**(**r**) and/or rotated through some angle θ about any axis, **v**.

With this general definition, we can summarize the different classes of planar defects:

- *Translation boundary, RB.* Any translation **R**(**r**) is allowed, θ is zero, and both regions are identical and thus perfectly aligned. Stacking faults (SFs) are a special case. We'll denote the translation boundary as RB so as to avoid confusing it with the twin boundary (TB).
- *Grain boundary, GB.* Any values of **R**(**r**), **n**, and θ are allowed, but the chemistry and structure of the two grains must be the same. The SF is again a special case, but this class also includes TBs.
- *Phase boundary, PB.* As for a GB, but the chemistry and/or structure of the two regions can differ.
- *Surface.* A special case of a PB where one phase is vacuum or gas.

Now with each of these groups, we can have special examples. We list some of the most common examples in Table 24.1, including those that we will consider in this chapter. For a more detailed discussion, we refer you to the general references at the end of the chapter.

RBs include the familiar SFs found in fcc, hcp, diamond-cubic, and layer materials. They have been widely studied because they play an important role in the mechanical properties of the fcc metals, e.g., Cu and stainless steel. They are also found in more complex materials such as spinels, Ni_3Al, Ti_3Al, etc., where the lattice parameters, and therefore the dislocation Burgers vectors, are large.

For example, the anti-phase boundary (APB) in ordered CuAu (which we can describe as two interpenetrating simple-cubic superlattices) is produced by translating one superlattice by ½<111> with respect to the other. It is called an APB because one superlattice is out of phase with the other. If the crystal were disordered and the Cu and Au occupied the bcc sites randomly, then ½<111> would be a lattice vector and no defect would exist. This particular APB can thus be regarded as an SF. Although we know that {111} is the favored SF plane for fcc metals, SFs in other materials lie on different planes. We will find that the methods used to characterize RBs can often be used to determine **R**(**r**) in other interfaces.

GBs fall into two groups, low-angle and high-angle. Low-angle boundaries necessarily involve a rotation which is usually accommodated by arrays of dislocations; we'll consider these defects in Chapter 25. High-angle boundaries can adopt some special values of **n** and θ such that a large fraction of lattice sites in one grain is shared by the other grain. We characterize the fraction by its inverse, which we call Σ. For example, the common twin boundary in fcc metals is the Σ = 3 grain boundary. The reason this is important to our discussion is that if a set of lattice points is common to two grains (as implied by the Σ coincident-site lattice concept), then certain planes may also be common and may give rise to common reflections. These reflections will remain common even if one grain is translated relative to the other. In that case, we'll have a special type of RB, called the rigid-body translation. Rigid-body translations in grain boundaries behave just like other SFs except **R** is usually small and is not directly related to the lattice parameters.

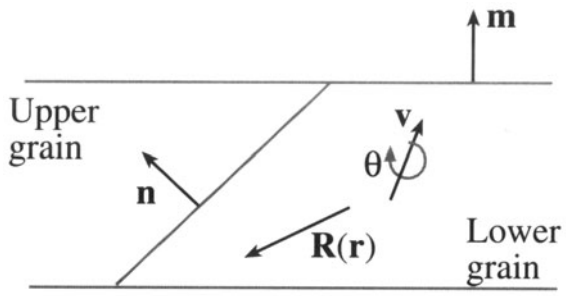

Figure 24.1. A specimen containing a planar defect. The lower grain is translated by a vector **R**(**r**) and rotated through an angle θ about the vector **v**, relative to the upper grain. The defect plane is **n**, the foil normal is **m**.

There is a second group of APBs where the two grains cannot be related by a translation. These occur in GaAs, ZnO, AlN, and SiC, for example. One lattice can always be related to the other by a rotation of 180° to give the equivalent of an inversion; they are sometimes known as inversion domain boundaries (IDBs). These special interfaces can often be imaged because of the small associated translation. We analyze this translation as if it were a simple RB because all the planes on one side of the IDB are parallel to their counterparts on the other; the $(hk\ell)$ plane on one side is parallel to the $\bar{h}\bar{k}\bar{\ell}$ on the other. We can't distinguish **g** from $\bar{\mathbf{g}}$ unless we use CBED (Taftø and Spence 1982).

PBs are rarely analyzed fully. If the orientation, chemistry, and structure can all change on crossing the boundary, then not only will the reflections change, but all extinction distances will change too. Some special examples of such interfaces are hcp-Co/fcc-Co, bcc-Fe/fcc-Fe, $NiO/NiFe_2O_4$, and $GaAs/Al_xGa_{1-x}As$. Of course, the number of other such interfaces is countless.

Surface studies using TEM have quite recently become very important although the experimental tools have been available for some time. We will discuss surfaces in this chapter insofar as they are imaged by diffraction contrast. So-called profile imaging will follow in Chapter 28 on HRTEM. The two surface-sensitive techniques are plan-view and reflection electron microscopy (REM; see Chapter 31).

24.2. WHY DO TRANSLATIONS PRODUCE CONTRAST?

As usual, we will start our analysis considering only two beams, O and G. Our approach will use hand-waving arguments, which are not perfect, to justify adapting the Howie–Whelan equations for specimens containing interfaces. We'll use the same approach for other defects in Chapter 25. Because the Howie–Whelan equations for perfect crystals assume two-beam conditions, we are able to solve them analytically. We'd like to be able to do the same when defects are present, because this gives us a physical understanding of the processes which produce the contrast. There are two important features which we will need to keep in mind:

- Diffraction contrast only occurs because we have Bloch waves in the crystal. However, our analysis will initially only consider diffracted beams.
- We make the column approximation so we can solve the equations; we must be wary whenever the specimen or the diffraction conditions change within a distance comparable to the column diameter.

A unit cell in a strained crystal will be displaced from its perfect-crystal position so that it is located at position $\mathbf{r}'_n$ instead of $\mathbf{r}_n$, where n is included to remind us that we are considering scattering from an array of unit cells; we'll soon omit the n.

Table 24.1. Examples of Internal Planar Defects

Group	Structure	Example	Example
SF	Diamond-cubic, fcc, zinc blende	Cu, Ag, Si, GaAs	**R** = ⅓ [111] or **R** = ⅙ [11$\bar{2}$]
APB/IDB	Zinc blende, wurtzite	GaAs, AlN	inversion
APB	CsCl	NiAl	**R** = ½ [111]
APB/SF	Spinel	$MgAl_2O_4$	**R** = ¼ [110]
GB	All materials	Often denoted by Σ where Σ^{-1} is the fraction of coincident lattice sites	rotation plus **R**
PB	Any two different materials	Sometimes denoted by Σ_1,Σ_2, which are not equal	rotation plus **R** plus misfit

$$\mathbf{r}'_n = \mathbf{r}_n + \mathbf{R}_n \qquad [24.1]$$

In this expression, $\mathbf{R}_n$ is actually $\mathbf{R}_n(\mathbf{r})$; it can vary throughout the specimen. The term $e^{2\pi i\mathbf{K}\cdot\mathbf{r}}$ in equation 13.3 now becomes $e^{2\pi i\mathbf{K}\cdot\mathbf{r}'}$ so we need to examine the term $\mathbf{K}\cdot\mathbf{r}'$. We know that $\mathbf{K}$ is $\mathbf{g} + \mathbf{s}$, so we can write

$$\begin{aligned}\mathbf{K}\cdot\mathbf{r}'_n &= (\mathbf{g}+\mathbf{s})\cdot(\mathbf{r}_n+\mathbf{R}_n)\\ &= \mathbf{g}\cdot\mathbf{r}_n + \mathbf{g}\cdot\mathbf{R}_n + \mathbf{s}\cdot\mathbf{r}_n + \mathbf{s}\cdot\mathbf{R}_n\end{aligned} \qquad [24.2]$$

Now, since $\mathbf{r}_n$ is a lattice vector, $\mathbf{g}\cdot\mathbf{r}_n$ is an integer as usual. The third term, $\mathbf{s}\cdot\mathbf{r}_n$, gives our usual sz term, so the new terms are $\mathbf{g}\cdot\mathbf{R}_n$ and $\mathbf{s}\cdot\mathbf{R}_n$.

When we discuss strong-beam images we know that $\mathbf{s}$ is very small. Since we are using elasticity theory, $\mathbf{R}_n$ must be small. Hence we ignore the term $\mathbf{s}\cdot\mathbf{R}_n$. Remember that we have made a special assumption which may not be valid in two situations:

- When $\mathbf{s}$ is large; we'll encounter this when we discuss the weak-beam technique in Chapter 26.
- When the lattice distortion, $\mathbf{R}$, is large; this occurs close to the cores of some defects.

We now modify equation 13.8 intuitively to include the effect of adding a displacement from equation 24.2

$$\frac{d\phi_{\mathbf{g}}}{dz} = \frac{\pi i}{\xi_0}\phi_{\mathbf{g}} + \frac{\pi i}{\xi_{\mathbf{g}}}\phi_0 \exp\left[-2\pi i(sz + \mathbf{g}\cdot\mathbf{R})\right] \qquad [24.3]$$

and

$$\frac{d\phi_0}{dz} = \frac{\pi i}{\xi_0}\phi_0 + \frac{\pi i}{\xi_{\mathbf{g}}}\phi_{\mathbf{g}} \exp\left[+2\pi i(sz + \mathbf{g}\cdot\mathbf{R})\right] \qquad [24.4]$$

Next, we simplify these equations just as we did in Chapter 13 by setting

$$\phi_0(z)_{(\text{sub})} = \phi_0 \exp\left(\frac{-\pi i z}{\xi_0}\right) \qquad [24.5]$$

and

$$\phi_{\mathbf{g}}(z)_{(\text{sub})} = \phi_{\mathbf{g}} \exp\left(2\pi i s z - \frac{\pi i z}{\xi_0}\right) \qquad [24.6]$$

Then the Howie–Whelan equations become

$$\frac{d\phi_{0(\text{sub})}}{dz} = \frac{\pi i}{\xi_{\mathbf{g}}}\phi_{\mathbf{g}(\text{sub})} \exp\left(2\pi i \mathbf{g}\cdot\mathbf{R}\right) \qquad [24.7]$$

and

$$\frac{d\phi_{\mathbf{g}(\text{sub})}}{dz} = \frac{\pi i}{\xi_{\mathbf{g}}}\phi_{0(\text{sub})} \exp\left(-2\pi i \mathbf{g}\cdot\mathbf{R}\right) + 2\pi i s \phi_{\mathbf{g}(\text{sub})} \qquad [24.8]$$

These equations are just as before (equations 13.14 and 13.15) but with the addition of the $2\pi i\mathbf{g}\cdot\mathbf{R}$ term. This additional phase is termed α, hence planar defects are seen when $\alpha \neq 0$

$$\alpha = 2\pi \mathbf{g}\cdot\mathbf{R} \qquad [24.9]$$

These expressions will be particularly useful in two cases:

- When $\mathbf{R}$ = constant.
- Understanding phasor diagrams when defects are present.

We start with a simple stacking fault lying parallel to the surface, as shown in Figure 24.2. In this situation the beams propagate through the upper layer just as if no fault were present. At a depth $z = t_1$, the beams may experience a phase change due to the effect of the translation $\mathbf{R}$, but after that they again propagate as if in a perfect crystal.

In this chapter, we'll see several values of α. A special case occurs when $\alpha = \pm 120°$. This value of α is often encountered since it occurs for fcc SFs. We'll also encounter the case where $\alpha = \pm 180°$; this value arises for some special APBs which are really SFs.

24.3. THE SCATTERING MATRIX

This discussion of the scattering matrix introduces no new concepts. It is just a different way of writing the equations

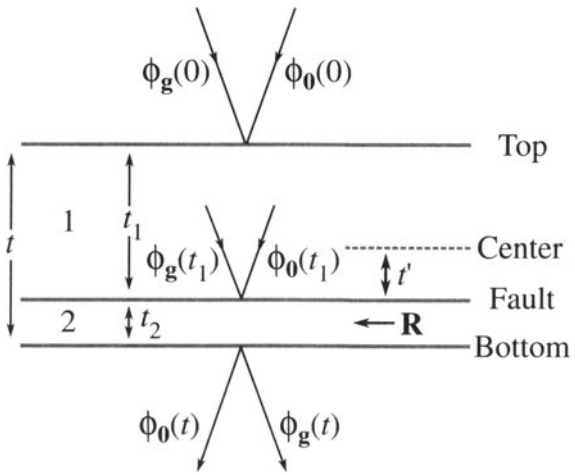

Figure 24.2. A stacking fault lying at depth t_1 in a parallel-sided uniformly thick specimen. The total thickness is t and $t_2 = t - t_1$.

so that, if you are calculating the image contrast, you can program the computer more easily, especially when you have complicated arrays of lattice defects. Our reason for delaying the introduction of the scattering matrix until now is that it is much easier to understand when you can apply it to a specific problem.

In equation 13.20, we showed that in the two-beam case, we can write these simple expressions for ϕ_0 and ϕ_g

$$\phi_0 = C_0 e^{2\pi i\gamma z} \qquad [24.10]$$

and

$$\phi_g = C_g e^{2\pi i\gamma z} \qquad [24.11]$$

Since there are two values for γ, we can express both the **0** and **g** beams as the combination of these two contributions to give

$$\phi_0(z) = C_0^{(1)}\psi^{(1)}\exp\left(2\pi i\gamma^{(1)}z\right) + C_0^{(2)}\psi^{(2)}\exp\left(2\pi i\gamma^{(2)}z\right) \qquad [24.12]$$

$$\phi_g(z) = C_g^{(1)}\psi^{(1)}\exp\left(2\pi i\gamma^{(1)}z\right) + C_g^{(2)}\psi^{(2)}\exp\left(2\pi i\gamma^{(2)}z\right) \qquad [24.13]$$

where the $\psi^{(i)}$ terms tell us the relative contributions of the $\gamma^{(1)}$ and $\gamma^{(2)}$ terms. (We are really saying that both Bloch waves contribute to both the **0** and **g** beams.) We can rewrite equations 24.12 and 24.13 in a matrix form

$$\begin{pmatrix}\phi_0(z)\\ \phi_g(z)\end{pmatrix} = \begin{pmatrix}C_0^{(1)} & C_0^{(2)}\\ C_g^{(1)} & C_g^{(2)}\end{pmatrix}\begin{pmatrix}\exp\left(2\pi i\gamma^{(1)}z\right) & 0\\ 0 & \exp\left(2\pi i\gamma^{(2)}z\right)\end{pmatrix}\begin{pmatrix}\psi^{(1)}\\ \psi^{(2)}\end{pmatrix} \qquad [24.14]$$

We can express our boundary conditions as

$$C_0^{(1)}\psi^{(1)} + C_0^{(2)}\psi^{(2)} = \phi_0(0) \qquad [24.15]$$

and

$$C_g^{(1)}\psi^{(1)} + C_g^{(2)}\psi^{(2)} = \phi_g(0) \qquad [24.16]$$

which we can now rewrite as

$$\begin{pmatrix}C_0^{(1)} & C_0^{(2)}\\ C_g^{(1)} & C_g^{(2)}\end{pmatrix}\begin{pmatrix}\psi^{(1)}\\ \psi^{(2)}\end{pmatrix} = \begin{pmatrix}\phi_0(0)\\ \phi_g(0)\end{pmatrix} \qquad [24.17]$$

(We actually saw in Section 13.9 that $\phi_0(0)$ is 1 and $\phi_g(0)$ is 0, because $z = 0$ is the top surface.) Now we can use matrix algebra to solve equation 24.17. First rewrite it as

$$C\begin{pmatrix}\psi^{(1)}\\ \psi^{(2)}\end{pmatrix} = \begin{pmatrix}\phi_0(0)\\ \phi_g(0)\end{pmatrix} \qquad [24.18]$$

then rewrite equation 24.18 as

$$\begin{pmatrix}\psi^{(1)}\\ \psi^{(2)}\end{pmatrix} = C^{-1}\begin{pmatrix}\phi_0(0)\\ \phi_g(0)\end{pmatrix} \qquad [24.19]$$

where C^{-1} is just the inverse matrix. Remember that the order is important in matrix multiplication and that $C^{-1}C = I$, the unit matrix.

Therefore we can rewrite equation 24.14 as

$$\begin{pmatrix}\phi_0(z)\\ \phi_g(z)\end{pmatrix} = C\begin{pmatrix}\exp\left(2\pi i\gamma^{(1)}z\right) & 0\\ 0 & \exp\left(2\pi i\gamma^{(2)}z\right)\end{pmatrix}C^{-1}\begin{pmatrix}\phi_0(0)\\ \phi_g(0)\end{pmatrix} \qquad [24.20]$$

Finally, we can define a new matrix $P(z)$ as the scattering matrix for a slice of thickness z

$$P(z) = C\begin{pmatrix}\exp\left(2\pi i\gamma^{(1)}z\right) & 0\\ 0 & \exp\left(2\pi i\gamma^{(2)}z\right)\end{pmatrix}C^{-1} = C\,\Gamma\,C^{-1} \qquad [24.21]$$

The matrix $P(z)$ thus gives us the values of the exit wave amplitudes at the bottom of the slice in terms of the incident values. In other words, the matrix $P(z)$ includes all the information to describe the propagation of the beams through the crystal; $P(z)$ is a *propagator* matrix. Notice that z only enters the equation through the Γ matrix in equation 24.21.

24.4. USING THE SCATTERING MATRIX

Now we illustrate the real strength of the scattering matrix approach by considering the effect of a planar fault lying parallel to the foil surface, as we saw in Figure 24.2. The idea is that we now have two slices of material of thickness t_1 and t_2. We can easily calculate $\phi_0(t_1)$ and $\phi_g(t_1)$ using equation 24.20. These values for ϕ_0 and ϕ_g then become the incident values for slice 2. The effect of the translation **R** is to multiply the terms in C_g in the lower slice by a phase factor exp $(-i\alpha)$, where $\alpha = 2\pi\mathbf{g}\cdot\mathbf{R}$ as usual. The matrix C for slice 2 is then written as

$$C_2 = \begin{pmatrix}C_0^{(1)} & C_0^{(2)}\\ C_g^{(1)}\exp(-i\alpha) & C_g^{(2)}\exp(-i\alpha)\end{pmatrix} \qquad [24.22]$$

We can write down the expression for $\phi_0(t)$ and $\phi_g(t)$ as

$$\begin{pmatrix} \phi_0(t) \\ \phi_g(t) \end{pmatrix} = C_2 P(t_2) C_2^{-1} C_1 P(t_1) C_1^{-1} \begin{pmatrix} \phi_0(0) \\ \phi_g(0) \end{pmatrix} \quad [24.23]$$

where the subscripts on C_1 and C_2 just identify the slices. Normally, this equation goes straight into the computer. However, we'll go back and consider a few special points:

- Look at equation 24.23 and set $\mathbf{R} = 0$, so that $C_1 = C_2$. You can see that $P(t) = P(t_1)P(t_2)$. Clearly we could cut the perfect-crystal specimen into many slices and $P(t)$ would always be the product of the scattering matrices for each slice.
- How do we prove equation 24.22? From equation 14.12 we know that a Bloch wave can be written as

$$b(\mathbf{k}) = \sum_{\mathbf{g}} C_{\mathbf{g}}(\mathbf{k}) \exp\left(2\pi i(\mathbf{k}+\mathbf{g})\cdot\mathbf{r}\right) \quad [24.24]$$

If the crystal is displaced by a vector $\mathbf{R}$ then we replace $\mathbf{r}$ with $\mathbf{r} - \mathbf{R}$ (notice the sign, see Section 25.14). (We have just used a "hidden" column approximation.) Equation 24.24 is then written

$$b(\mathbf{k}) = \sum_{\mathbf{g}} C_{\mathbf{g}}(\mathbf{k}) \exp\left(2\pi i(\mathbf{k}+\mathbf{g})\cdot(\mathbf{r}-\mathbf{R})\right) \quad [24.25]$$

$$b(\mathbf{k}) = e^{-2\pi i\mathbf{k}\cdot\mathbf{R}} \sum_{\mathbf{g}} C_{\mathbf{g}}(\mathbf{k})\, e^{-2\pi i\mathbf{g}\cdot\mathbf{R}}\, e^{2\pi i(\mathbf{k}+\mathbf{g})\cdot\mathbf{r}} \quad [24.26]$$

C_0 is not affected by $\mathbf{R}$ since $2\pi\mathbf{0}\cdot\mathbf{r} = 0$, but C_g is multiplied by $e^{-i\alpha}$.

- If you choose the coordinates appropriately (see Chapter 14) then C is a unitary matrix. In this case, you can find C^{-1} just by reflecting across the diagonal and taking the complex conjugate of each term. This *trick* will allow you to express equation 24.23 explicitly, as given by Hirsch *et al.* (1977) (omitting a phase factor)

$$\begin{aligned} &\varphi_0(t) = \\ &[\cos(\pi\Delta kt) - i\cos(\beta)\sin(\pi\Delta kt)] \\ &+ \tfrac{1}{2}(e^{i\alpha}-1)\sin^2\beta\cos(\pi\Delta kt) - \tfrac{1}{2}(e^{i\alpha}-1)\sin^2\beta\cos(2\pi\Delta kt') \end{aligned} \quad [24.27]$$

$$\begin{aligned} &\varphi_g(t) = i\sin\beta\sin(\pi\Delta kt) \\ &+ \tfrac{1}{2}\sin\beta\left(1-e^{(-i\alpha)}\right)\left[\cos\beta\cos(\pi\Delta kt) - i\sin(\pi\Delta kt)\right] \\ &- \tfrac{1}{2}\sin\beta\left(1-e^{(-i\alpha)}\right)\left[\cos\beta\cos(2\pi\Delta kt') - i\sin(2\pi\Delta kt')\right] \end{aligned} \quad [24.28]$$

In equations 24.27 and 24.28, t' is the distance of the fault below the center of the slice, i.e., we define $t' = t_1 - t/2$ where t_1 lies between 0 and t. (It's a good, but tedious, exercise to derive these equations for yourself.) The right-hand side of equations 24.27 and 24.28 each contains three terms:

- The first term is just what we found in Chapter 13 where the phase factor $\alpha = 0$, i.e., it's just like the perfect crystal.
- The second term is independent of the position of the planar fault because it doesn't depend on t'.
- The third term depends on t' such that both ϕ_0 and ϕ_g change with a periodicity in t' given by Δk^{-1}. So these amplitudes show the same dependence on ξ_g^{eff}. They will both show thickness variations.

You should keep in mind that we derived these equations for a planar defect lying parallel to the parallel surfaces of our specimen and normal to the beam. We can now take these ideas and apply them to planar defects which are inclined to the surface, by calculating the contrast for all values of t' between 0 and t. The important points to remember are:

- The model used in the calculation was a flat interface parallel to the surface of a platelike specimen. You'll see fault fringes when t' varies across the fault, but you don't usually have to consider the fact that either the surface or the fault may be inclined to the beam.
- The concept of the scattering matrix allows you to identify very clearly the effect of the defect on ϕ_0 and ϕ_g.

24.5. STACKING FAULTS IN fcc MATERIALS

We'll begin our discussion of actual examples with the SF in fcc materials. Before we discuss the details of contrast from SFs in fcc materials, we'll summarize the important results which hold for all planar defects:

- The appearance of the image depends on the specimen thickness.
- Pairs of BF/DF SF images are not generally complementary even though we are using a two-beam approximation. Compare to the complementary behavior of the thickness fringes discussed in Chapter 23.

- Planar defects can, in fact, have a thickness. We'll illustrate this concept using overlapping faults in fcc materials (see also Section 6.6).

Do not assume all faults are the same as in fcc materials!

24.5.A. Why fcc Materials?

There are several reasons for emphasizing the analysis of stacking faults in fcc crystals:

- Many important materials are fcc, including the metals Cu, Ag, Au, and austenitic stainless steel, and the semiconductors Si, Ge, and GaAs.
- Most of the analysis of SFs derives from the study of fcc materials.
- The translations are well known and directly related to the lattice parameter: **R** is either $\frac{1}{6}\langle\bar{1}\bar{1}2\rangle$ or $\frac{1}{3}\langle 111\rangle$. Notice that these definitions differ by the lattice vector, $\frac{1}{2}\langle 110\rangle$. (Actually there may be small deviations from these ideal values, but we'll ignore them for now.)

We want to learn how to extend this analysis to other fault vectors and avoid making unfounded assumptions when we do extend it. The geometry often encountered is shown in Figure 24.3. If the sample is single crystal, then you need to prepare a specimen with a [111] foil normal, so that you can image long segments of the dislocations lying in the plane of the foil on their (111) glide plane.

You should note that $(11\bar{1})$ is one of three possible planes for an inclined SF. In this case, the translation at the stacking fault will be $\mathbf{R} = \pm\frac{1}{3}[11\bar{1}]$; the phase factor, α, is $2\pi\,\mathbf{g}\cdot\mathbf{R}$. If you form an image with the $\mathbf{g} = (2\bar{2}0)$ reflection strongly excited, then $\mathbf{g}\cdot\mathbf{R} = 0$ and the fault is out of contrast in both BF and DF. If, instead, you use the reflection $\mathbf{g} = (02\bar{2})$, then $\mathbf{g}\cdot\mathbf{R} = \frac{1}{3}$ or $-\frac{1}{3}$ and $\alpha = \frac{8\pi}{3} = \frac{2\pi}{3} = 120°$ or $-\frac{8\pi}{3} = -\frac{2\pi}{3} = -120°$ (modulo 2π in each case). Notice that if the stacking fault lies parallel to the surface of this (111)-oriented specimen, you must tilt the specimen to see *any* contrast from the SF, i.e., $\mathbf{g}\cdot\mathbf{R} = 0$ for all values of **g** lying in the fault plane.

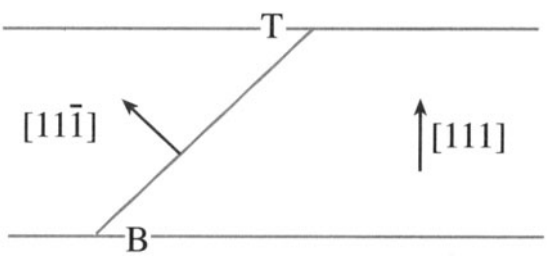

Figure 24.3. A stacking fault in a parallel-sided fcc specimen. The normal to the specimen is [111] and the normal to the SF is [11$\bar{1}$]. T and B indicate the top and bottom of the foil.

Figures 24.4A–D show two typical BF/DF pairs of $\pm\mathbf{g}$ strong-beam images from the same SF. In the BF images the outer fringes are the same on both sides of the fault (both gray or both white) while in the DF images one outer fringe is white but the other is gray, as summarized in Figures 24.4E and F. The questions which arise are:

- What determines whether a fringe will be gray or white?
- Why are the two images not complementary?

Note in Figures 24.4E and F that Type A reflections are 200, 222, and 440 while Type B are 111, 220, and 400.

24.5.B. Some Rules

There are some experimental rules:

- Be very careful when you record such a pair of images: record the DP for each image. Be sure to note which of the two bright spots corresponds to the direct beam.
- Use the same strong $hk\ell$ reflection for BF and DF imaging. Therefore, to form the CDF image using a strong $hk\ell$ reflection you must first tilt the specimen so that $\bar{h}\bar{k}\bar{\ell}$ is strong, and then use the beam tilts to move $hk\ell$ onto the optic axis where it will become strong (see Section 22.5). This is confusing, so we recommend that you sacrifice a little image resolution and compare the BF image with a displaced-aperture DF image, rather than a CDF image.

In a modern IVEM, there is almost no loss of resolution between displaced-aperture DF and CDF.

So to avoid the possibility of confusion about which reflection to use for the DF image (e.g., see Edington 1976, p. 148), just displace the aperture to the strong $hk\ell$ reflection in every case.

This is exactly the opposite of the approach used by Edington, who advocates tilting in $\bar{h}\bar{k}\bar{\ell}$ for the DF image, which reverses the DF contrast in Figures 24.4E and F. Our approach ensures that diffraction from the same $hk\ell$ planes causes the contrast in both BF and DF images.

Then there are some rules for interpreting the contrast:

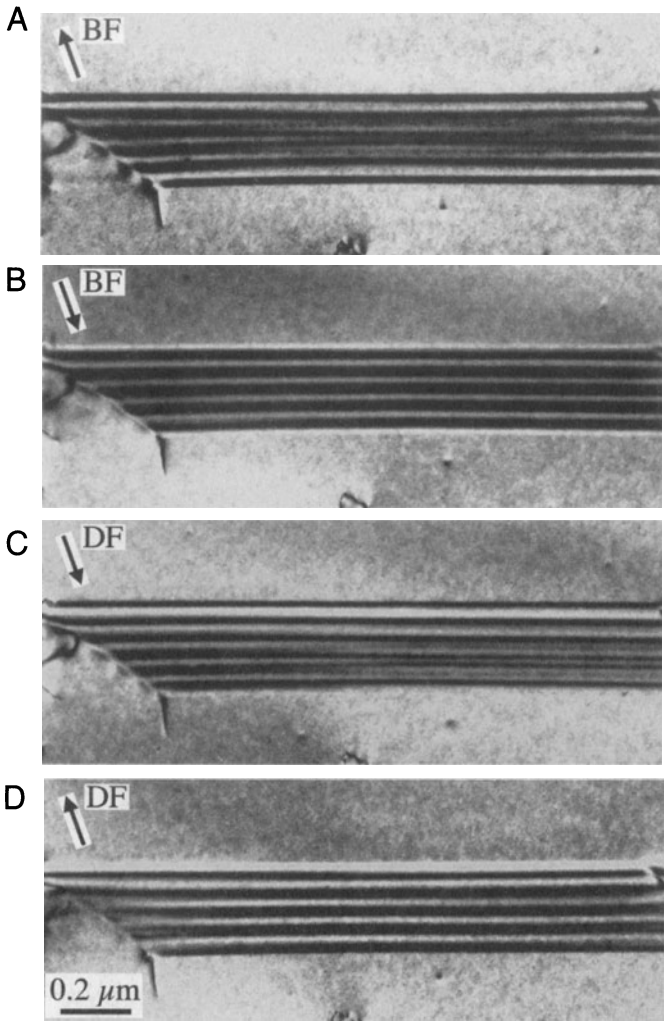

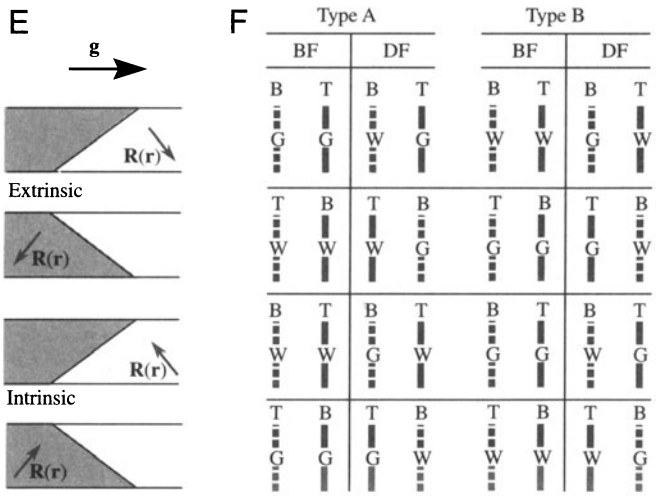

Figure 24.4. (A–D) Four strong-beam images of an SF recorded using ±**g** BF and ±**g** DF. The beam was nearly normal to the surfaces; the SF fringe intensity is similar at the top surface but complementary at the bottom surface. The rules are summarized in (E) and (F) where G and W indicate that the first fringe is gray or white, and (T,B) indicates top/bottom.

- In the image, as seen on the screen or on a print, the fringe corresponding to the top surface (T) is white in BF if $\mathbf{g}\cdot\mathbf{R}>0$ and black if $\mathbf{g}\cdot\mathbf{R}<0$.
- Using the same strong $hk\ell$ reflection for BF and DF imaging, the fringe from the bottom (B) of the fault will be complementary whereas the fringe from the top (T) will be the same in both the BF and DF images.
- The central fringes fade away as the thickness increases. If this seems anomalous, the explanation is in Section 24.10.
- The reason it is important to know the sign of **g** is that you will use this information to determine the sign of **R**.
- For the geometry shown in Figure 24.3, if the origin of the **g**-vector is placed at the center of the SF in the DF image, the vector **g** points away from the bright outer fringe if the fault is extrinsic and toward it if it is intrinsic (200, 222, and 440 reflection); if the reflection is a 400, 111, or 220 the reverse is the case.
- Don't forget that, as we said at the start of Chapter 22, any contrast must be >~5–10% to be visible to the eye, so any intensity change due to $\mathbf{g}\cdot\mathbf{R}$ effects is only detectable if $\mathbf{g}\cdot\mathbf{R}>0.02$ (unless you can digitize and process your analog TEM image). With experience, you'll find there is an optimum thickness to view defect contrast, before absorption effects make it difficult. You must also carefully select **s** so the background intensity in the matrix around the defect is gray and this maximizes visibility of lighter and darker fringes.

So just because you can't see a defect doesn't mean it isn't there, or that $\mathbf{g}\cdot\mathbf{R} = 0$.

As we said, these complex rules are summarized in Figures 24.4E and F. Although they are very useful, in practice you should remember that they were derived for a very special combination of **R** and **g** in fcc materials. Some important examples of $\mathbf{g}\cdot\mathbf{R}$ are given in Table 24.2. As we'll describe in Section 24.11, you should use a computer program to check the contrast.

24.5.C. Intensity Calculations

Now let's consider intensity calculations using the column approximation, which we briefly discussed in Section 13.11. If the fault cuts the column at a depth t_1, we can deduce from equations 24.22 and 24.23 that

Table 24.2. Values of g·R for Some Common R/g Combinations

	R	**g**	$\alpha = 2\pi\,\mathbf{g}\cdot\mathbf{R}$ (mod 2π)
SF in fcc	$\frac{1}{3}[111]$	$(11\bar{1})$, (220), $(\bar{1}\bar{1}3)$	$2\pi/3$
SF in fcc	$\frac{1}{3}[111]$	(113)	$4\pi/3$
Translation at APB in Fe_3Al	$\frac{1}{2}[110]$	(100)	π
Small **R**, e.g., NiO	any	**g** or **s** or ξ_g differ slightly	δ

$$\phi_g = \frac{i\pi}{\xi_g}\left\{\int_0^{t_1} e^{-2\pi isz}dz + e^{-i\alpha}\int_{t_1}^{t} e^{-2\pi isz}dz\right\} \qquad [24.29]$$

which gives

$$\phi_g = \frac{i\pi}{s\xi_g} e^{-2\pi ist_1}\{\sin(\pi st_1) + e^{-i\alpha}\sin(\pi s(t-t_1))\} \qquad [24.30]$$

We rearrange equation 24.30 to give an expression for the intensity, I_g (= $\phi_g\phi_g^*$). This rearrangement involves a little manipulation

$$I_g = \frac{1}{(s\xi_g)^2}\left\{\sin^2\left(\pi st_1 + \frac{\alpha}{2}\right) + \sin^2\left(\frac{\alpha}{2}\right) - \sin\left(\frac{\alpha}{2}\right)\sin\left(\pi st + \frac{\alpha}{2}\right)\cos(2\pi st')\right\} \qquad [24.31]$$

where $t' = t_1 - t/2$ as before. So the contrast depends on both the thickness and the depth. Note that $t/2$ is the center of the foil. Since α is fixed for a particular defect, let's fix t. Then equation 24.31 becomes

$$I_g \propto \frac{1}{s^2}\{A - B\cos(2\pi st')\} \qquad [24.32]$$

Now we have cosine depth fringes or defect thickness fringes, just as we did for the perfect crystal.

- The thickness periodicity depends on s^{-1}.
- The intensity varies as s^{-2}.

We could have derived this equation from equation 24.28 with more work. However, the value of the scattering matrix approach is that we don't derive the analytical expression but just run the computer.

In Chapter 26 we will discuss this SF contrast in terms of phasor diagrams, which give a graphical way to represent these equations.

24.5.D. Overlapping Faults

It is interesting to extend this analysis to the case of overlapping faults. Taking the analytical approach, we can extend equation 24.29 to the case of two overlapping faults, the first at depth t_1 and the second at depth t_2

$$\phi_g = \frac{i\pi}{\xi_g}\left\{\int_0^{t_1} e^{-2\pi isz}dz + e^{-i\alpha}\int_{t_1}^{t_1+t_2} e^{-2\pi isz}dz + e^{-i(\alpha_1+\alpha_2)}\int_{t_1+t_2}^{t} e^{-2\pi isz}dz\right\} \qquad [24.33]$$

An experimental illustration of a somewhat more complex situation, involving several overlapping SFs, is shown in

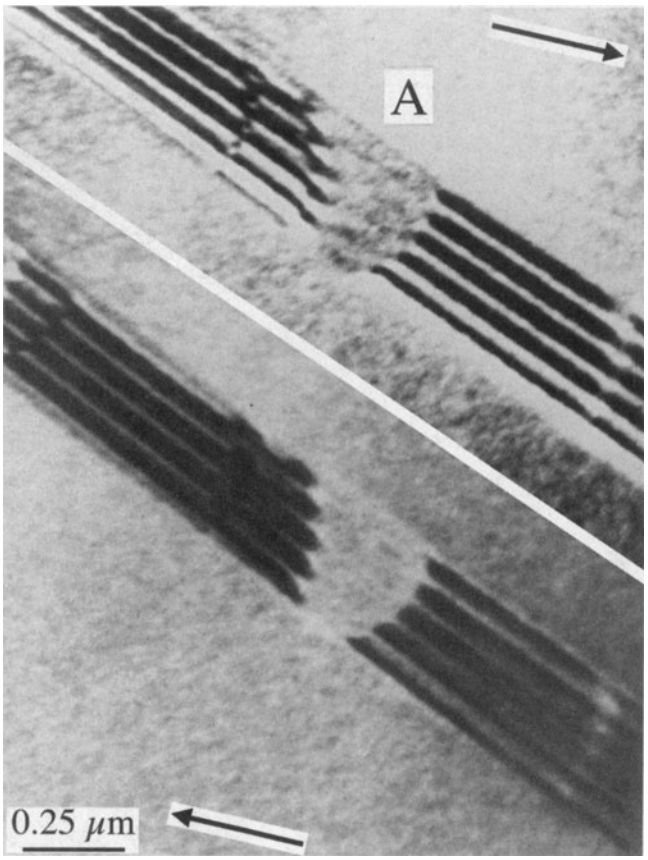

Figure 24.5. Two ±**g** BF images of overlapping SFs in fcc steel, with the direction of **g** indicated. The faults are very close together. When three faults overlap the effective value of **R** is 0 so the contrast disappears.

Figure 24.5. We can see two very interesting features in this image:

- The BF/DF contrast is not complementary.
- It sometimes appears that there is no contrast, even when we know that there are overlapping SFs. This can happen if, e.g., three SFs overlap on adjacent (or nearly adjacent) planes; then the effective **R** can be $3 \times \frac{1}{3}[11\bar{1}]$, which is a perfect lattice vector and can therefore appear to give $2\pi\mathbf{g}\cdot\mathbf{R} = 0$.

We will return to this topic in Section 26.6 where we'll show that some planar defects, such as the extrinsic SF in Si or the dissociated {112} twin boundary in some fcc metals, really have a thickness. We can then analyze the contrast from such interfaces using the overlapping-fault model.

24.6. OTHER TRANSLATIONS: π AND δ FRINGES

We discussed the $L1_0$ structure of NiAl in Section 16.5. This intermetallic is an example of a large group of materials which can contain a different type of RB. If the Ni atoms sit at the corners of the cell in one crystal region but the Al atoms sit at the corners in another part of the crystal, then the two crystal regions are related by a translation of $\frac{1}{2}[111]$. The two crystals would otherwise still be perfectly aligned but are separated by this RB, which we call an APB.

Similarly in the $L1_2$ structure of the intermetallic Ni_3Al, we could have the Al atoms on the corners of the unit cell in one part of the crystal and displaced by $\mathbf{R} = \frac{1}{2}[110]$ in the adjacent region. (We can actually form six nonequivalent APBs in this structure.) The crystal structure looks like fcc but the Al atoms are at the corners of the unit cell (forming the simple-cubic superlattice) with the Ni at the face-centered positions. The easy way to appreciate this RB is to think what would happen if the alloy were completely disordered: there would be no planar defect. This RB can be imaged using the (100) reflection. Notice again that for a disordered structure, the {100} reflections would be absent if the alloy were disordered; the {100} planes are said to give rise to superlattice reflections; these reflections would be forbidden if the material were disordered. For this case we can readily show that the phase factor $\alpha = \pi$, so the fringes we see are called π fringes. The structure of this interface is shown schematically in Figure 24.6. These π fringes can give symmetric fringes in DF and BF and complementary BF/DF pairs.

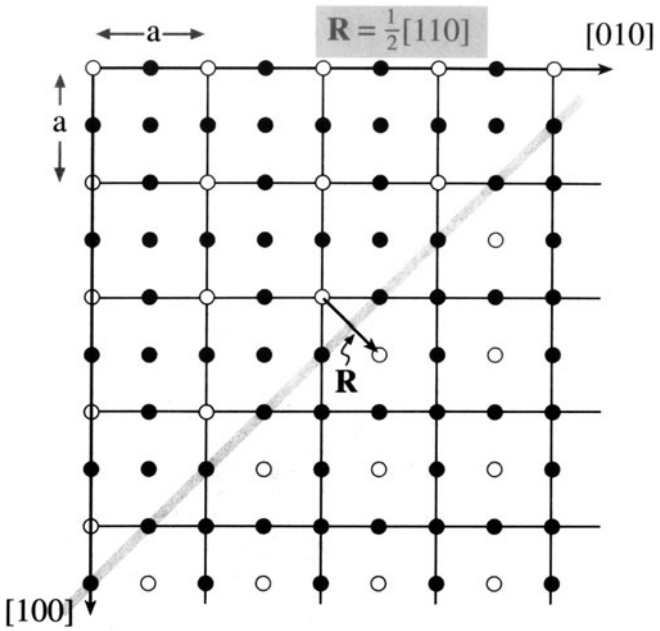

Figure 24.6. Schematic of an interface in the intermetallic Ni_3Al showing how the two structures link coherently. The phase factor at such an interface is π and the fringes seen in the image are called π fringes.

Similar RBs are very common in oxides because the unit cell is often quite large, giving more opportunities to form such interfaces. The interface shown in Figures 24.7A and B has been called both an SF and an APB in the spinel. These interfaces can show all the features we discussed in Section 24.5 for SFs in fcc materials, and those we've just discussed depend on which reflection you use. You can again see a change in contrast in Figure 24.7C when APBs in TiO_2 overlap as shown schematically in Figure 24.7D (Amelinckx and Van Landuyt, 1978). In Figures 24.7A,B, if you image the fault using the 220 reflection $2\pi\mathbf{g}\cdot\mathbf{R} = \pi$ and so you'll see SF fringes. If however, you image using 440, $2\pi\mathbf{g}\cdot\mathbf{R} = 2\pi$, so you'll only see residual contrast (because **R** is not exactly $\frac{1}{4}[101]$.

The APB shown in Figure 24.8 is different yet again. This planar defect in GaAs is also known as an IDB (Section 24.1). The fringes you see are caused by a translation, but **R** is not related in a simple way to the structure of the crystal (Rasmussen *et al.* 1991). As shown in the diagram, the translation is present because there is a small relaxation of the Ga-Ga and As-As bonds at this {110} interface. The value of **R** was determined to be 0.19Å with a statistical uncertainty of ±0.03Å. These fringes are then known as δ fringes (because they are only small transla-

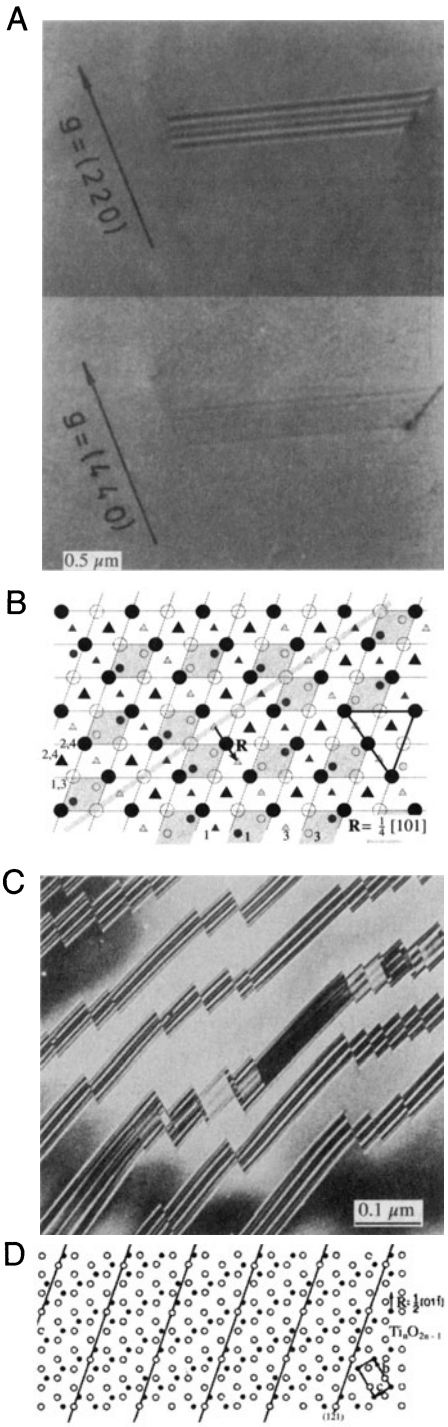

Figure 24.7. (A) Pair of BF images and (B) schematic of an SF in spinel; this interface is also known as an APB since the SF translation vector is a perfect (sub)lattice vector in the underlying fcc oxygen sublattice as shown in (B). Large circles are O anions at different heights (1,3) and (2,4); the small circles and triangles are cations at different heights (1–4 as indicated). (C) APBs can overlap just as SFs can as shown by these faceted APBs in TiO_2. Many of the facets give quite similar contrast but those near the center are strikingly different because of overlap. The schematic (D) shows a series of APBs, each of which is formed by a translation which has little effect on the oxygen sublattice.

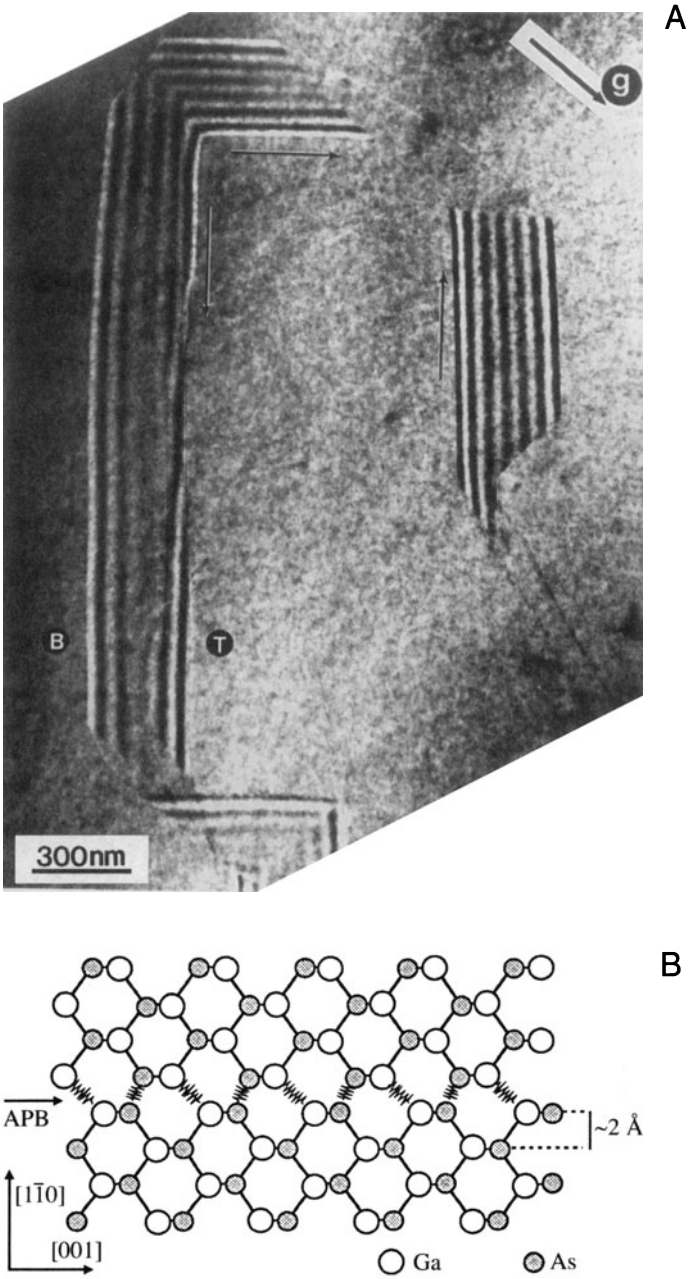

Figure 24.8. (A) A faceted APB (or IDB) in GaAs with (B) a schematic of the (1$\bar{1}$0) facet. The translation is caused by the difference in length of the Ga-Ga and As-As bonds and does not correspond to any length in the GaAs lattice.

tions and are not related in a simple way to 2π). The use of image-simulation programs, which are necessary to determine **R** (remember that the wavelength of the 200-kV electrons used for the measurement is itself 0.025Å), is discussed in Section 24.13.

Table 24.3. Examples of Special Phase Boundaries

Boundary	Example of material	Features
Ferromagnetic domain boundaries	NiO	
Ferroelectric/piezoelectric boundaries	$BaTiO_3$	Small tetragonal distortion
Composition boundary	GaAs/AlGaAs	ξ_g is different on two sides of boundary, even for perfect lattice matching
Structure boundaries	α-SiC/β-SiC	
	hcp-Co/fcc-Co	
Composition/structure	Nb/Al_2O_3	
	Al/Cu	
	α-Fe/Fe_3C	

24.7. PHASE BOUNDARIES

We list a few special phase boundaries in Table 24.3.

An example of a PB is shown in Figure 24.9. In NiO, which is ferromagnetic, some of the planes rotate when the structure changes from cubic symmetry below the Curie temperature. Now we can also define the cubic structure as rhombohedral with $\alpha = 60°$ in the rhombohedron. Below the Curie temperature, the rhombohedral angle is distorted by only 4.2′ from the true 60°. Therefore, most **g**-vectors will rotate through a very small angle and hence produce a change in the value of **s**. However, as you can see in Figure 24.9, this small rotation can readily be detected by the change in contrast and the faint fringes at the phase boundary.

We can have overlapping PBs, so the warning is the same: be very wary and use tilting experiments.

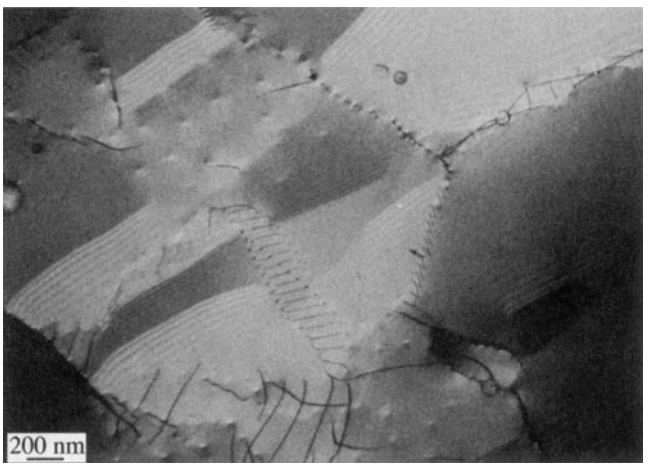

Figure 24.9. The ferromagnetic material NiO undergoes a structural change from cubic to distorted rhombohedral at the Curie temperature. Although the distortion in the rhombohedral structure is very small, it causes a detectable rotation of the lattice planes which results in the δ fringes in the image.

24.8. ROTATION BOUNDARIES

What can we learn about rotation boundaries when the rotation angle is greater than about 0.1°? Unfortunately, the answer is "not a lot," unless we have defects which accommodate the rotation. Then we are into the subject of diffraction contrast of line defects in interfaces. However, with care you may be able to excite **g** in one grain or in both by tilting the specimen. The difficulty, of course, is that $\mathbf{s}_g$ is likely to be different in each material. Complications will also arise if other defects are present, since you may or may not see those defects. Examples of such interfaces are shown in Figure 24.10.

24.9. DIFFRACTION PATTERNS AND DISPERSION SURFACES

You read in Chapter 17 that what you see in an image must be related to what happens in the DP, which in turn is determined by how the Ewald sphere intersects the reciprocal lattice. Figure 17.5 showed that a planar defect which is inclined to the surface of a parallel-sided specimen will give rise to relrods. Therefore, a planar defect in a parallel-sided specimen will produce at least two spots in the diffraction pattern. Since most specimens are wedges (see Figure 17.4), and the planar defect will, in general, be inclined to both surfaces, the relrod geometry is even more complex. Figure 24.11 shows lines normal to each interface and their associated relrods. You can appreciate that when the Ewald sphere cuts these relrods, several spots may appear in the diffraction pattern. Now we need to relate these relrods to the fringes we see in the image. This model would predict that we would not produce fringes when $\mathbf{s} = 0$, so we should modify what we did in Figure 17.15. The periodicities of the fringes in the image are inversely related to the distances (M_1N, and M_2N) between the spots in the DP.

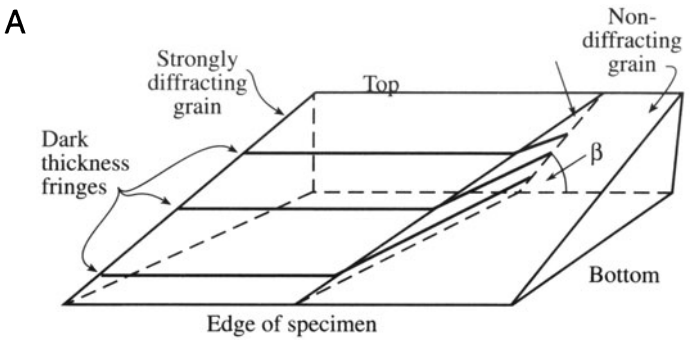

Figure 24.10. (A) If the adjoining grains are rotated so that they do not share a common reflection, images can be formed where only one of the grains diffracts. As shown in (B), the thickness fringes associated with the wedge-shaped foil merge into the thickness fringes associated with the inclined interface. (C) If the foil is tilted so that the same (though not coincident) reflection is excited in both grains, the number of fringes in the interface increases with each incremental increase in the wedge thickness.

At **s** = 0, the fringe spacing is determined by $\Delta k = \xi_g^{-1}$; the spacing of the fringes is ξ_g.

When a planar defect is present in the specimen, the two branches of the dispersion surface are not only coupled

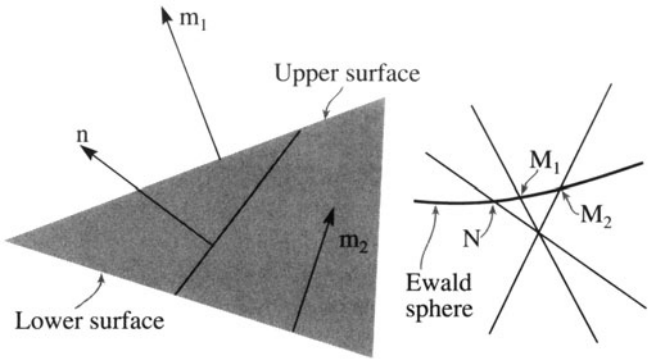

Figure 24.11. In a wedge specimen, the planar defect will, in general, be inclined to both surfaces and the relrod geometry is complex. The fringe spacing in the image is related to the reciprocal of the distances M_1N and M_2N.

along a tie line normal to the surface of the specimen but also along that normal to the planar defect. However, when **s** = 0, the thickness periodicity in the image corresponds to the extinction distance. When we relate this to the region G in the reciprocal lattice, the two relrods (which are a kinematical construction) must actually separate to give the two hyperbolas shown in Figure 24.12, which is why we drew Figures 17.15 and 23.6 as we did.

If you see fringes in the image, spots will be present in the DP.

The spots in the DP are associated with points M and N in Figures 24.11 and 24.12.

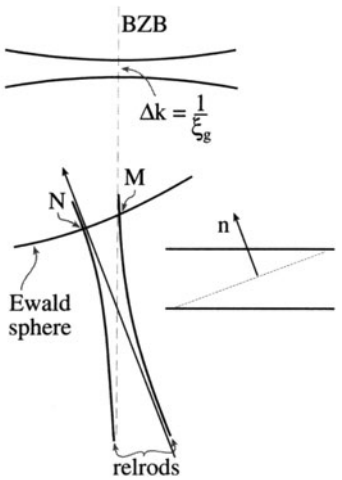

Figure 24.12. The dispersion-surface construction for an inclined planar defect in a parallel-sided specimen. (Compare with Figures 17.15 and 23.6.) For simplicity, we show the hyperbolas due to the defect alone, not the extra effects that would arise in a wedge specimen.

24.10. BLOCH WAVES AND BF/DF IMAGE PAIRS

In Chapter 14 we saw that, in a crystal, the electron must propagate as Bloch waves, and yet we have not mentioned Bloch waves in our discussion of thickness and bending so far. Most of the analysis of this topic is beyond the scope of this text, but it is important to understand the basic ideas, particularly since they will also apply to scattering from defects in the crystals. Remember that ξ_g is a direct consequence of having two Bloch waves. The important message here is: don't let the words overawe you.

The idea is quite simple. Since we have two Bragg beams excited, then we must have two Bloch waves in the crystal. The propagation vectors of these two waves are $\mathbf{k}_1$ and $\mathbf{k}_2$, with the difference $|\Delta\mathbf{k}|$ being given by s_{eff}. We see a thickness dependence in the image because the two waves are interfering. The only two waves which are really present in the crystal are the two Bloch waves. It's the beating of these two waves which gives rise to thickness effects.

In the two-beam case, the Bloch waves, 1 and 2, are channeled along and between the atom columns (see Figure 14.2). A fault may change the channeled wave into the nonchanneled one, as you can see in Figure 24.13. The effect of the planar defect is simply to couple the Bloch waves; in other words, the defect links the different branches of the dispersion surface. The noncomplementary contrast at SFs in fcc metals is directly explained by this coupling.

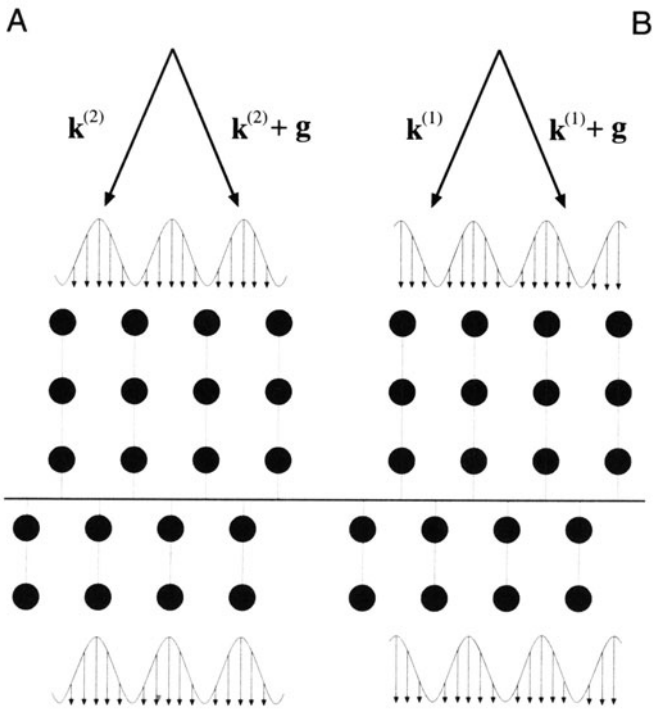

Figure 24.13. Bloch waves 1 and 2 are channeled along and between the atom columns, respectively, until they meet the fault. There the atomic columns are translated so that the channeled Bloch wave may become the nonchanneled one.

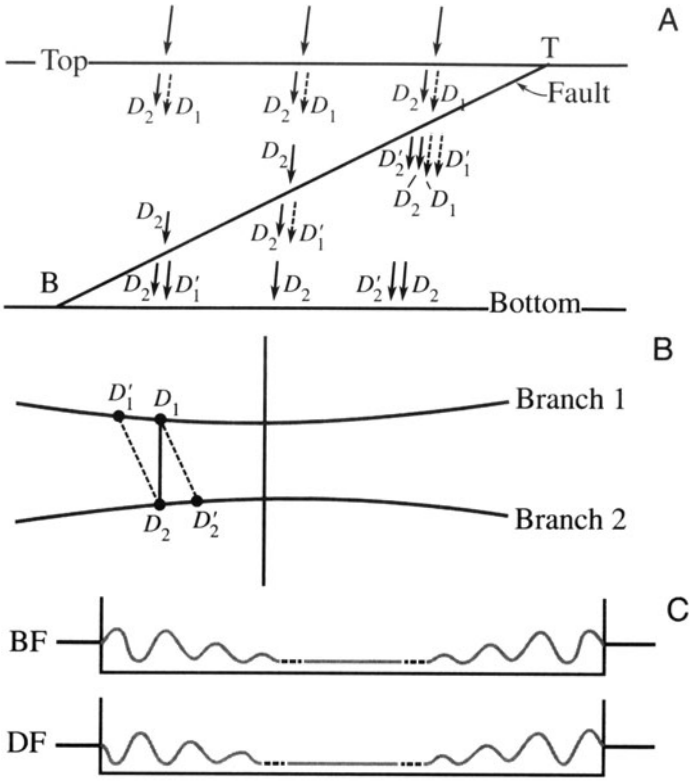

Figure 24.14. The absorption of the branch-1 Bloch wave near the top surface, T, of the specimen and its re-creation when the planar defect is near the bottom, B, determines the contrast we see. (A) shows which Bloch waves are present at the different depths in the specimen, (B) shows how the Bloch waves are coupled along tie lines joining the two branches of the dispersion surface, and (C) shows the resulting contrast.

As soon as the beam enters the specimen we excite Bloch waves 1 and 2. Therefore, in Figure 24.14A, the two Bloch waves 1 and 2 are shown everywhere at the top surface of the foil. The planar defect links points D_1 and D_2 on the two branches of the dispersion surface, as shown in Figure 24.14A, along the tie line, D_1D_2' and $D_1'D_2$. We'll analyze the three situations shown in Figure 24.14B, which correspond to the planar defect being close to the top, the middle, and the bottom of the specimen. The key feature is that, as we saw in Section 14.6, Bloch wave 1, which has the larger **k**-vector, will be preferentially absorbed. It is actually totally absorbed in thicker specimens.

■ When the planar defect is close to the top surface (as occurs near T), waves 1 and 2 are both coupled (or scattered) to the other branch of

the dispersion surface so we form four Bloch waves (but with only two **k**-vectors). Both Bloch waves which are associated with the upper branch of the dispersion surface (wave vector $\mathbf{k}_1$) are preferentially absorbed, but the waves D_2 and D_2' both reach the lower surface. There, they interfere to give the thickness fringes even though they are both associated with the lower branch of the dispersion surface; D_2' retains a "memory" of D_1.

- When the fault is close to the middle of the specimen, the branch-1 Bloch wave is absorbed before it reaches the planar defect but a new Bloch wave D_1' is formed at the defect. However, while traversing the other half of the foil, this wave is also absorbed so that only wave D_2 reaches the lower surface. Thus the electrons can propagate through the specimen (we can see through it) but there are no thickness fringes, because only one Bloch wave survives. However, we can still image defects in these thicker areas, as you'll see if you look back at Figure 23.10.
- At the lower surface, B, only wave D_2 survives to reach the planar defect but it now produces a new wave D_1', which can reach the lower surface, recombine with Bloch wave D_2, and produce thickness fringes. The resulting contrast is summarized in Figure 24.14C.

Bloch-wave absorption is a critical factor in explaining the appearance of contrast from planar defects. The part of this argument which is not intuitive is the fact that D_2' retains a memory of D_1; this memory allows it to interfere with D_2 to produce the thickness fringes near the top of the specimen, even though no Bloch wave from branch 1 reaches the bottom of the specimen. We'll refer you to the article by Hashimoto *et al.* (1962) for further discussion on this topic.

24.11. COMPUTER MODELING

From the discussion in Sections 24.5 and 24.6, you will realize that α and π fringes are usually understandable as long as you know what the defect is, and as long as it's not actually a set of overlapping defects. The contrast from δ fringes is much more complex and combinations of α, π, and δ fringes are difficult! The situation will become even more complicated if you want to understand the contrast occurring when other defects interact with these planar faults. A computer program is then really the only way to analyze the contrast from these defects.

The first program to attempt the task of simulating two-dimensional images of planar defects is described in the book by Head *et al.* (1973) (see Section 1.5). One of several modern approaches is Comis, a Unix program, which is also available in a Macintosh version. We will mention some of the features of these programs to help you select one, but leave the detailed descriptions to the appropriate manuals. The most important reason for using any program must be your desire to understand the contrast and thus characterize the defect.

> These programs are tools to assist you toward the goal of quantitative analysis of diffraction contrast, but you always need the fully quantitative experimental image, too.

You need an accurate simulation of the image you see in the microscope. The fact that the image varies with depth, thickness, **g**-vector, etc., is actually to your advantage, since you then have many variables, all of which you must be able to measure to achieve a good match with your experimental image. From the point of view of quantitative analysis, a one-dimensional line (intensity) profile is as valid as a two-dimensional image. Of course, if you can compare the contrast in an image and a simulation point by point, then you can have much greater confidence in the matching. The two-dimensional simulated image is also more viewer-friendly!

A great advantage of more powerful computers is that you can also test the effect of specimen geometry more readily. Thus, for example, Viguier *et al.* (1994) have shown using the Cufour simulation package (Schäublin and Stadelmann 1993) that the rules for fringe contrast given by Gevers *et al.* (1963) will not work if the specimen is tilted such that it intersects the bottom of the foil above the point where it intersects the top! You can understand this situation more easily by looking at the specimen geometry shown in Figure 24.15.

Image simulation tells us that $\mathbf{g}\cdot\mathbf{R}$ must be >0.02 to produce visible fringes, and you don't need to know the local structure at the planar defect when determining this condition. You could, in principle, detect smaller values of **R** by using larger **g**-vectors, but in practice it then becomes more difficult to set up a well-defined diffraction geometry.

The next two sections are rather specialized and you may wish to leave them until much later, especially if you don't have access to a suitable program, or until you are prepared to write your own. Do consult the key references and list of available programs in Section 1.5 before writing your own program. The subject is just as relevant to the topics of Chapters 25 and 26, but we include it in this

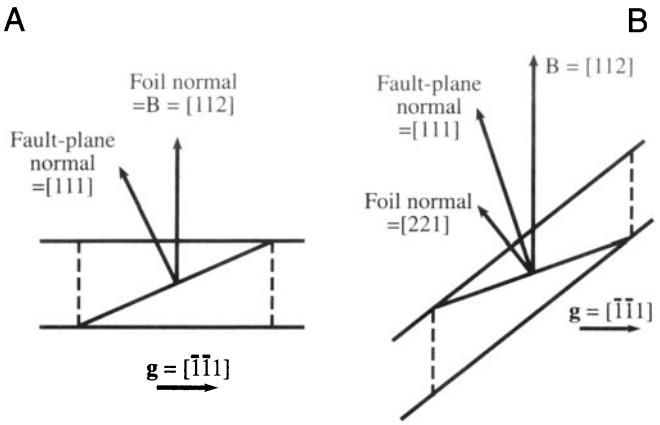

Figure 24.15. Many of the "rules" for predicting the contrast from planar "defects" make certain assumptions about the geometry of the defect relative to the surface of the specimen which may not always hold. Here it is demonstrated that the intersection of the planar defect with the upper specimen surface may be lower than the intersection with the bottom surface. This geometry can cause a reversal in the rules.

chapter mainly because the analysis of planar defects is the most straightforward application.

24.12. THE GENERALIZED CROSS SECTION

Head *et al.* (1973) presented a method and a computer program for the computation of BF and DF images of line and planar defects. The source code is given in their book and is available from the WWW. You should note several important features of this program:

- It uses the two-beam theory of electron diffraction.
- It uses the column approximation.
- The simulated image can be displayed as a halftone image rather than as intensity profiles.

This program was so successful, in part, because Head *et al.* were able to calculate the images quite quickly in spite of the fact that the computers available to microscopists were often not particularly powerful in ~1970. The calculations used a concept which they called the *generalized cross section* (GCS). (The GCS is not a scattering cross section, it is actually a slice through the specimen.) The GCS can be used when the displacement field, $u_{\mathbf{k}}$, satisfies the requirement that

$$u_{\mathbf{k}}(x, y, z) = u_{\mathbf{k}}(x, 0, z + cy) \qquad [24.34]$$

Here, c is a constant and the foil is imagined to be laterally infinite. When this requirement is satisfied, the calculation of $u_{\mathbf{k}}$ is greatly simplified. One such situation is the important case where several dislocations and their associated fault planes are all parallel to one another. Then you only need to calculate the many-beam Howie–Whelan equations on the plane $y = 0$. The displacement field for two columns y_1 and y_2 will only differ by a translation along the column, i.e., the z-direction. You don't want to repeat calculations you've already done; just calculate the image on a mesh in the x-y plane.

Examples of comparisons between experimental and simulated images using Comis are shown in Figure 24.16. This package is particularly attractive since it also performs elasticity calculations for simple defect configurations. You'll also find it instructive for simulating the effect of changing different parameters, such as:

- Change the accelerating voltage to see the extinction distances change.
- Change the absorption parameters to see the loss of SF-fringe contrast near the middle of the foil ($z = 0.5t$).

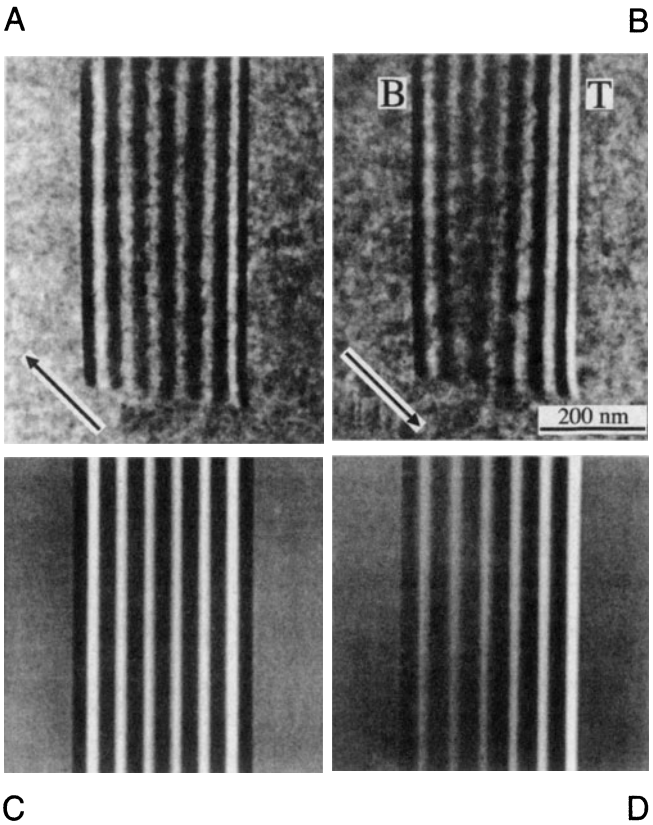

Figure 24.16. (A) Experimental BF image of an APB with **g** = 220. (B) DF image of the same defect, **g** = $\bar{2}20$. (C,D) Corresponding simulated images.

- Change the number of beams contributing to the image; how good is your two-beam assumption?
- Look at how reversing **g** changes the geometry of the image.
- Compare BF and DF as you vary the value of $\mathbf{s}_g$.

24.13. QUANTITATIVE IMAGING

One of the important applications of diffraction-contrast images is the detailed characterization of defects. With the improvements in the TEM, particularly in resolution and drift, we are now able to pay more attention to the fine structure of defects and this requires *quantitative* image analysis. In particular, we need to use the actual intensity levels in the image. One obstacle for quantitative analyses has been the uncertainty in the background-level intensity caused by inelastic scattering. As energy-filtered images become more widely available (see Chapter 40) this problem will disappear. Direct digital recording of the intensities, using a CCD camera, will also make a quantitative analysis more tractable, eliminating uncertainties associated with the calibration of the response of the emulsion of the photographic film. (See also Section 30.4.)

With these new applications of diffraction-contrast images in mind, improved simulation programs have become essential. An ideal program will be versatile, but user-friendly; it will allow you not only to calculate the image but also give defect-interaction geometries. In simulating images of crystal defects you'll encounter several problems which are almost independent of one another. You must:

- Define the geometry of the defects and of the specimen (the diffracting conditions).
- Calculate the displacement field associated with the defects.
- Propagate and scatter the electron beams throughout the foil (i.e., solve the Howie–Whelan equations).

We've already discussed the theoretical basis of the diffraction process, so we'll now illustrate some of the numerical methods which you can employ for different defect geometries. In Chapter 25 we'll consider other types of defects which may be analyzed, methods for defining them, and how you can calculate the displacement field.

24.13.A. Theoretical Basis and Parameters

We'll use the Comis program as an example of the considerations which go into a simulation program. One message which you should certainly understand from this discussion is that you must be very cautious when using any program to simulate images. All such programs make assumptions and simplifications.

> As always, when using the computer to simulate TEM images: beware of the black box. Don't automatically believe everything that comes out of it.

Comis is based on the Howie–Whelan dynamical theory of electron diffraction and therefore neglects diffuse scattering. We'll follow the approach given by Howie and Basinski (1968).

- Use the deformable-ion approximation to describe how the crystal is influenced by the displacement field, **R**. In this model, the potential at **r** in the deformed crystal is assumed to be equal to the potential at the point $\mathbf{r} - \mathbf{R}(\mathbf{r})$ in the perfect crystal. The model is good unless $\mathbf{R}(\mathbf{r})$ varies too rapidly.
- Extend the Howie–Whelan approach to many beams and avoid the column approximation.

The resulting equations are basically the same as those we derived in Chapter 13, so don't be put off by their appearance.

> We are now including terms which allow for a variation in *x* and *y*: these terms were specifically excluded in Chapter 13 when we made the column approximation.

The equations are now written as

$$\frac{\partial \phi_{\mathbf{g}}(r)}{\partial z} = i\pi \sum_{\mathbf{h}} \left(\frac{1}{\xi_{\mathbf{g}-\mathbf{h}}} + \frac{i}{\xi'_{\mathbf{g}-\mathbf{h}}} \right) \phi_h e^{2\pi i \left(\left(s_{\mathbf{h}} + s_{\mathbf{g}} \right) z - (\mathbf{h}-\mathbf{g}) \cdot \mathbf{R} \right)} \quad [24.35]$$

$$\theta_x \frac{\partial \phi_{\mathbf{g}}}{\partial x} - \theta_y \frac{\partial \phi_{\mathbf{g}}}{\partial y} + \frac{i}{4\pi\chi_z} \left(\frac{\partial^2 \phi_{\mathbf{g}}}{\partial x^2} + \frac{\partial^2 \phi_{\mathbf{g}}}{\partial y^2} \right)$$

As usual, χ is the incident-beam wave vector in vacuum, **g** is a particular diffraction vector, and **h** represents all the other possible diffraction vectors; you might like to compare this

equation with equation 13.8. We have defined two new parameters to take account of the direction of the beam

$$\theta_x = \frac{(\chi + \mathbf{g})_x}{\chi_z} \quad \text{and} \quad \theta_y = \frac{(\chi + \mathbf{g})_y}{\chi_z} \qquad [24.36]$$

The x-y plane in the reciprocal lattice contains the dominant reflections, and z is almost parallel to the incident beam. The number of beams you can include in the calculation is limited only by the capacity of your computer. The standard default for a program would be to select only beams on the systematic row. However, nonsystematic beams can substantially influence your image, so it is useful if you can include sets of beams which are coplanar with the systematic row. We define the deviation of the crystal orientation from the exact Bragg condition by specifying the wave-vector components χ_x and χ_y; the latter applies when reflections outside the systematic row are included. Now we can calculate *all* the deviation parameters, $\mathbf{s}_\mathbf{h}$; there are many beams and each $\mathbf{s}$ can be different.

Each extinction distance $\xi_\mathbf{g}$ is defined as the ratio $\chi_\mathbf{g}/|U_\mathbf{g}|$, as usual with $U_\mathbf{g}$ being a Fourier component of the perfect-crystal potential. The Fourier components can be calculated from X-ray scattering factors, using the Mott expression (Mott and Massey 1965). For most situations the scattering angle is small enough, so the X-ray scattering factors may, in turn, be calculated using the nine-parameter Gaussian fit given by Doyle and Turner (1968).

You'll need to know the unit cell for your material and the Debye–Waller factors. Comis, for example, can then automatically calculate $\xi_\mathbf{g}$ using a built-in table of the Doyle–Turner parameters. The Debye–Waller factor (B) is related to the (mean-square) vibrational amplitude of an atom on a lattice site. So it is a temperature-sensitive term. You need to know B if you want to convert X-ray structure factors to electron structure factors (or vice versa) at a given temperature, or if you want to compare structure factor measurements taken at different temperatures. When you calculate extinction distances, the Debye–Waller factors are essential to determine the effect of temperature.

Equation 24.35 is only valid if your crystal has a center of symmetry, otherwise you have to redefine $\xi_\mathbf{g}$. Simulations involving noncentrosymmetric crystals can be performed, but you have to replace the $\xi_\mathbf{g}$ and $\xi_\mathbf{g}'$ with complex quantities and then defining all the parameters is really difficult (Gevers *et al.* 1966) (see also equation 14.2).

You can take account of absorption effects in the usual way by adding imaginary Fourier components, $U_\mathbf{g}'$(Yoshioka 1957); the absorption distances, $\xi_\mathbf{g}'$, are then defined as we discussed in Section 23.8. There are equations which a program can use to estimate the absorption distances, e.g., the linear relation $|U_\mathbf{g}'|/|U_\mathbf{g}| = a + b|\mathbf{g}|$, as suggested by Humphreys and Hirsch (1968), or you could specify each individual absorption distance directly.

24.13.B. Apparent Extinction Distance

The program developed by Head *et al.* was based on the two-beam approximation. The success of such calculations relies on the fact that $\xi_\mathbf{g}$ may be replaced by an apparent extinction distance, $\xi_\mathbf{g}^a < \xi_\mathbf{g}$. This substitution compensates for scattering into beams that are not included in the two-beam calculation. The term $\xi_\mathbf{g}^a$ depends on the t and must be estimated in each individual situation, e.g., by fitting the simulated image to your experimental image. For a quantitative image analysis it is important that you should have as few adjustable parameters as possible; using the many-beam program eliminates the need to use the parameter $\xi_\mathbf{g}^a$. Alternatively, you may determine $\xi_\mathbf{g}^a$ by comparing simulated thickness fringes calculated using many-beam and two-beam approximations.

24.13.C. Avoiding the Column Approximation

You can perform simulations with or without the column approximation. With the column approximation, you only keep the first term on the right-hand side of equation 24.35. The equations are reduced to a system of ordinary differential equations which the program must solve at each image point (x, y). In practice, the equation is solved on the nodes of a mesh (columns) using a fifth-order Runge–Kutta integration routine (which you, or the program, can look up when you need it). You need to choose the size and "resolution" of the mesh. As we'll see in Chapter 26, there are situations where the column approximation will not be acceptable (Howie and Sworn 1970).

Without the column approximation, equation 24.35 gives us a system of coupled partial differential equations. The boundary conditions (at $z = 0$) can be generally written in the form

$$a_\mathbf{g}\phi_\mathbf{g} + b_\mathbf{g}\frac{\partial\phi_\mathbf{g}}{\partial x} = c_\mathbf{g} \qquad [24.37]$$

where we're ignoring changes in the y-dimension.

You can use fixed boundary conditions (Howie and Basinski 1968):

- The foil is divided into thin slices of thickness Δz. You should not confuse this with the multislice method for lattice-image simulation which we'll see in Chapter 29; we are still using

Howie–Whelan equations. Then, equation 24.35 is integrated, using the column approximation, through the first slice, i.e., from $z = 0$ to $z = \Delta z$, at all the mesh points.

- The corrections to the column approximation, i.e., the terms containing derivatives with respect to x and y, are then evaluated by interpolation and included.
- The procedure is repeated until the exit surface of the foil is reached.

With this procedure, you are actually applying the column approximation to the outer boundary of the mesh. So, in equation 24.37, $a_g = 1$, $b_g = 0$, and $c_g = \phi_g$ at the initial surface. In order to avoid distortion of the image, you must choose the step size, Δz, carefully and be sure that the distance between columns (mesh size) is small enough (Anstis and Cockayne 1979).

24.13.D. The User Interface

You'll want to run your program interactively so it should include commands which allow you to change parameters easily. Ideally, it will allow you to access each command through the keyboard using a menu. In Comis, for example, certain standard menus are available for special purposes. The user can also build (and save) menus interactively. This allows all the relevant parameters and commands for a particular problem to be present within a single menu. At any time, all the commands are available through the keyboard.

Although typical simulations may be performed in a matter of seconds, many-beam calculations including several dislocations may require more CPU time. For this situation, Comis includes a "submit" command which will start a batch job based on your current data and parameters. Thus, the interactive mode may be used as a convenient way of submitting several jobs with varying parameter values.

For many problems, a purely visual comparison of experimental and simulated images is sufficient to allow you to interpret your image. In these situations you can often find a ξ_g^a such that the simulations can be carried out with only two beams (Head *et al.* 1973). However, since many parameters are involved in the image-matching process, it is best to eliminate as many unknown variables as possible. Many-beam calculations are even more important for quantitative analyses.

CHAPTER SUMMARY

The key points discussed in this chapter are:

- We see contrast from planar defects because the translation, **R**, causes a phase shift $\alpha = 2\pi \mathbf{g}\cdot\mathbf{R}$.
- In the two-beam case, we can derive analytical expressions to describe the contrast .
- We can use the scattering-matrix method in the two-beam case and can readily extend it to more complicated multibeam situations.

Many different types of planar defect can be studied. You should be careful not to assume that all defects behave the same as SFs in fcc materials.

There is a direct relationship between the information in the images and that in the DPs, which you can understand using the concept of the relrod.

You need to understand how Bloch waves behave to explain why BF/DF pairs of images are not complementary, and why the contrast from planar defects can disappear in the "middle" of the image. The latter is a result of preferential absorption of certain Bloch waves.

You can now use computer modeling of diffraction-contrast images of planar defects to perform quantitative analysis and image matching.

REFERENCES

General References

Amelinckx, S. and Van Landuyt, J. (1978) in *Diffraction and Imaging Techniques in Material Science,* **1** and **2** (Eds. S. Amelinckx, R. Gevers, and J. Van Landuyt), 2nd edition, p. 107, North-Holland, New York.

Christian, J.W. (1975) *The Theory of Transformations in Metals and Alloys,* Part 1, 2nd edition, Pergamon Press, New York.

Edington, J.W. (1976) *Practical Electron Microscopy in Materials Science,* Van Nostrand Reinhold, New York.

Forwood, C.T. and Clarebrough, L.M. (1991) *Electron Microscopy of In-*

terfaces in Metals and Alloys, Adam Hilger, New York. Invaluable for anyone studying interfaces by TEM.

Head, A.K., Humble, P., Clarebrough, L.M., Morton, A.J., and Forwood, C.T. (1973) *Computed Electron Micrographs and Defect Identification,* North-Holland, New York.

Rasmussen, D.R. and Carter, C.B. (1991) *J. Electron Microsc. Techniques* **18**, 429.

Sutton, A.P. and Balluffi, R.W. (1995) *Interfaces in Crystalline Materials,* Oxford University Press, New York.

Wolf, D. and Yip, S., Eds. (1992) *Materials Interfaces, Atomic-level Structure and Properties,* Chapman and Hall, New York.

Specific References

Anstis, G.R. and Cockayne, D.J.H. (1979) *Acta Cryst.* **A35**, 511.

Doyle, P.A. and Turner, P.S. (1968) *Acta Cryst.* **A24**, 390.

Gevers, R., Art, A., and Amelinckx, S. (1963) *Phys. Stat. Sol.* **3**, 1563.

Gevers, R., Blank, H., and Amelinckx, S. (1966) *Phys. Stat. Sol.* **13**, 449.

Hashimoto, H., Howie, A., and Whelan, M.J. (1962) *Proc. Roy. Soc. London* **A269**, 80.

Hirsch, P., Howie, A., Nicholson, R.B., Pashley, D.W., and Whelan, M.J. (1977) *Electron Microscopy of Thin Crystals,* 2nd edition, p. 225, Krieger, Huntington, New York.

Howie, A. and Basinski, Z.S. (1968) *Phil. Mag.* **17**, 1039.

Howie, A. and Sworn, H. (1970) *Phil. Mag.* **31**, 861.

Humphreys, C.J. and Hirsch, P.B. (1968) *Phil. Mag.* **18**, 115.

Mott, N.F. and Massey, H.S.W. (1965) *The Theory of Atomic Collisions,* 3rd edition, Clarendon Press, Oxford.

Rasmussen, D.R., McKernan, S., and Carter, C.B. (1991) *Phys. Rev. Lett.* **66**, 2629.

Schäublin, R. and Stadelmann, P. (1993) *Mater. Sci. Engng.* **A164**, 373.

Taftø, J. and Spence, J.C.H. (1982) *J. Cryst.* **15**, 60.

Thölen, A.R. (1970) *Phil. Mag.* **22**, 175.

Thölen, A.R. (1970) *Phys. Stat. Sol. (A)* **2**, 537.

Viguier, B., Hemker, K.J., and Vanderschaeve, G. (1994) *Phil. Mag.* **A69**,19.

Yoshioka, H. (1957) *J. Phys. Soc. Japan* **12**, 618.